Electronic materials

CrossMark

Magnetic hollow mesoporous carbon composites with impedance matching for highly effective microwave absorption

Guozhu Shen[1,2] , Junzhao Ren[1] , Bin Zhao[1] , Buqing Mei[1] , Hongyan Wu[1] , Xumin Fang[2] , and Yewen Xu[2,*]

[1] School of Physics and Optoelectronic Engineering, Nanjing University of Information Science and Technology, Nanjing 210044, China

[2] Science and Technology on Near-Surface Detection Laboratory, Wuxi 214035, China

ABSTRACT

Lightweight hollow mesoporous carbon spheres (HMCSs) with large air/carbon interface in the mesoporous shell and interior void have been successfully synthesized via a 'polymerization–pyrolysis–etching' route. The complex permittivity of the HMCSs can be easily adjusted by carbonization temperature in the frequency range of 2–18 GHz, which is in favor of designing absorbers in different frequency range. The minimum reflection loss value of -26.4 dB at 6.7 GHz with a thickness of 5.0 mm and the maximum effective absorption bandwidth (less than -10 dB) of 5.5 GHz can be gained for the HC-700/paraffin composite with only 10 wt% HMCSs and a thickness of 2.5 mm. To enhance the magnetic loss and improve the impedance matching of the HMCSs, electroless plating methods are employed to deposit Ni and Fe nanoparticles on the HMCSs. Benefiting from the dielectric loss, magnetic loss and impedance characteristic, the new lightweight Fe/HMCSs composite with 40 wt% HC–Fe shows superior microwave absorption properties. The stronger reflection loss can be obtained at all designed thicknesses, and the peak value of reflection loss is less than -20 dB at each thickness of greater than 1.2 mm. The minimum reflection loss reaches -49.7 dB at 13.0 GHz, and the effective absorption bandwidth is 4.0 GHz with a thickness of 1.6 mm. This research is providing a new insight in the preparation and design of lightweight microwave absorption materials.

Introduction

Nowadays, electromagnetic interference (EMI) and pollution are becoming more and more serious with the fast development of telecommunication and detection technologies [1–3]. In order to resolve the problems, considerable attention has been paid to electromagnetic wave absorbing materials, which can convert electromagnetic energy into thermal energy or dissipate them via interference. Prominent

Springer

https://doi.org/10.1007/s10853-018-3100-z

absorbing materials are required to have the properties of lightweight and powerful absorption in a wide frequency range. The electromagnetic wave absorption property mainly depends upon the complex permittivity, complex permeability and characteristic impedance of absorbing materials. Carbon materials with high dielectric loss have been paid significant attention due to lightweight, tunable permittivity and thermal and chemical stability [4–6]. However, carbon-absorbing materials with thin thickness are difficult to meet the demand of strong absorption in a wide frequency range because of the poor impedance matching resulting from their high complex permittivity and low complex permeability [7]. Thus, they are usually composited with some magnetic materials [8–12]. Currently, various magnetic carbon composites have been exploited and designed to attenuate microwave, such as magnetic carbon fiber [13–15], carbon nanotube [16–21], graphene [22–24], porous carbon [25–27] and core/shell carbon composites [28–30]. Among these carbon materials, porous carbons are the most prospective candidates of microwave absorption materials due to easy fabrication and surface modification [31–33]. The porous carbon materials including microporous carbon, mesoporous carbon and hollow carbon can be easily prepared by hard or soft template method [34–36]. The dynamic dielectric behaviors of the porous carbon materials were also investigated by many researchers in order to understand their dielectric loss mechanism and evaluate their electromagnetic wave absorption properties. Compared to the counterpart solid carbon particles, Zhou et al. [5] thought that enhanced microwave absorption of hollow carbon spheres resulted from well-matched impedance together with multiple reflection induced by the hollow structure. Xu et al. [37] concluded that excellent microwave absorption properties of mesoporous carbon hollow spheres are ascribed to the matching of characteristic impedance resulting from large carbon–air interface in the mesoporous shell and interior void. The similar conclusion was also made by Cheng et al. [38]. Microwave absorption properties of ordered mesoporous carbon, disordered mesoporous carbon and nonporous carbon studied by Du et al. [39] showed that graphitization degree is the primary factor affecting the microwave absorption and appropriate graphitization degree, pore structure and degree of order played important roles on microwave absorption. Huang et al. investigated the effect of pore morphology in carbon on dielectric loss in the case of similar graphitization degree. The results suggested that porous carbon with cage-like pores indicated a better capacity of dielectric loss than slit-shaped pores in the frequency range of 8.2–12.4 GHz [40]. However, to our knowledge, rare reports on the synergistic effect between dielectric loss and magnetic loss of hollow carbons decorated by magnetic nanoparticles are available in recent years.

Herein, we fabricated the monodisperse hollow mesoporous carbon spheres (HMCSs) with tunable complex permittivity by a one-pot and surfactant-free synthesis method. In order to improve the magnetic loss and impedance matching properties of the HMCSs, electroless plating methods were employed to deposit metal Ni and Fe on the HMCSs. The dynamic dielectric and magnetic behaviors of the HMCSs composites were discussed, and their microwave absorption properties were investigated in the frequency range of 2–18 GHz.

## Materials and methods

Materials

Tetrapropyl orthosilicate (TPOS) was purchased from Aladdin Industrial Corporation (Shanghai, China). Formaldehyde solution was provided by Xilong Chemical Co., Ltd. (Shantou, China), and other chemicals were purchased from Sinopharm Chemical Reagents Co., Ltd. (Shanghai, China). All chemicals were used as-received state.

Experiment

The preparation of magnetic HMCSs composites includes four steps: formation of $SiO_2@SiO_2/RF$ (resorcinol–formaldehyde resin) core–shell structures, carbonization, removal of SiO_2 by etching and electroless plating nickel or iron on HMCSs. The preparation route is illustrated in Fig. 1.

Synthesis of HMCSs

HMCSs were synthesized according to the method of Zhang [41]. In a typical synthesis, 13.84 mL of TPOS and 12 mL of $NH_3 \cdot H_2O$ (25 wt%) were added to the solution containing 280 mL of ethanol and 40 mL of
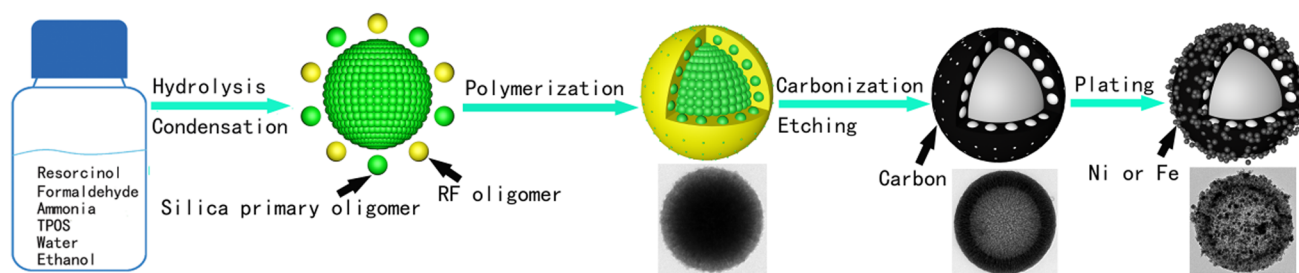
Figure 1 A schematic illustration of the preparation of HMCSs and their magnetic metal composites.

H_2O under stirring at room temperature. After 15 min, 1.6 g of resorcinol and 2.24 mL of formaldehyde (37%) were added to the above solution, and then, the system was kept stirring for 24 h. The resulting brown solid product was collected by centrifugation, washed with deionized water and ethanol and dried at 80 °C. The HMCSs were obtained by carbonization of the above solid product at 700 °C, 800 °C and 900 °C under N_2 flowing for 5 h with a heating rate of 2 °C/min and removal of SiO_2 via hydrofluoric acid (10 wt%). These obtained HMCSs were denoted as HC-700, HC-800 and HC-900 according to the carbonization temperature, respectively.

Preparation of magnetic HMCSs composites

Here the sample HC-800 was selected as an example to plate with nickel and iron based on measured electromagnetic parameters of HMCSs. Electroless Ni plating process is similar to Co plating as in our previous work [25]. Previous to electroless plating, 400 mg of HC-800 was sensitized and activated by $SnCl_2$/HCl and $PdCl_2$/HCl solution, respectively. Then, the sensitized and activated HC-800 was immersed in 150 mL plating bath containing 3.75 g of $NiCl_2 \cdot 6H_2O$, 3.75 g of $NaH_2PO_2 \cdot H_2O$, 4.50 g of Na_3-$C_6H_5O_7 \cdot 2H_2O$ and 6.00 g of NH_4Cl, and the pH of the plating solution was adjusted to 8.8 by $NH_3 \cdot H_2O$. Ni deposition was performed in a beaker at 80 °C by thermostat bath and stirred with a mechanical stirrer for 30 min. The resultant magnetic composite was separated by an external magnetic field, washed with deionized water and vacuum dried at 60 °C. Finally, heat treatment was conducted at 400 °C under argon for 3 h in order to improve its magnetic properties. 0.952 g of Ni/HC-800 composite was obtained, and it was denoted as HC–Ni.

For electroless Fe plating, as reported by Park [42], 400 mg of HC-800 was sensitized and activated as the above Ni plating. 150 mL of Fe plating solution was composed of 3.00 g of $FeCl_2 \cdot 4H_2O$, 13.50 g of $KNaC_4H_4O_6 \cdot 4H_2O$, 3.00 g of NaOH, 2.25 g of $NaBH_4$ and deionized water. Fe deposition was performed at 80 °C with mechanical stirring for 90 min. The obtained 1.333 g of magnetic Fe/HC-800 composite was collected and thermally treated as the above HC–Ni and denoted as HC–Fe.

The samples HC-700 and HC-900 were plated with Ni and Fe as the same as the above HC-800, and the products were denoted as HC-700–Ni, HC-700–Fe, HC-900–Ni and HC-900–Fe, respectively.

Characterization and measurement

The phase of the samples was inspected by X-ray diffraction (XRD, Thermo ARL X'TRA) using Cu-Kα radiation. The morphology and microstructure were examined on transmission electron microscopes (TEM, Phillips Tecnai 12 and FEI Tecnai G2 F30) and field-emission scanning electron microscope (FE-SEM, Hitachi SU-4800). The magnetic properties were measured by a vibrating sample magnetometer (VSM Lake Shore 7300). Nitrogen sorption isotherms were obtained at 77 K on a Quadrasorb SI (Quantachrome). Relative complex permittivity and permeability were measured using a vector network analyzer (VNA, Agilent E8363C). For measuring the electromagnetic parameters, the prepared HC-700, HC-800 and HC-900 powders were homogenously mixed with 90 wt% paraffin and the magnetic HMCSs composites powders were mixed with 60 wt% paraffin, respectively, and then pressed into a toroid with outer diameter of 7.0 mm and inner diameter of 3.0 mm.

Results and discussion

Structure and phase characterization

Figure 2 shows the XRD patterns of samples HC–Ni and HC–Fe. Three diffraction peaks at $2\theta = 44.5°$, $51.8°$ and $76.3°$ can be indexed to the (111), (200) and (220) planes of fcc-Ni (JCPDS 04-0850) for sample HC–Ni, indicating that Ni is the main phase. For sample HC–Fe, not only Fe but also Fe_3O_4 phase can be found. The peaks at $2\theta = 44.7°$ and $65.0°$ are indexed to the (110) and (200) planes of bcc-Fe (JCPDS 87-0721), respectively, and all other peaks can be indexed to different planes of fcc-Fe_3O_4 (JCPDS 89-0691). Although the stabilizer $KNaC_4H_4O_6·4H_2O$ is used in the Fe plating solution, Fe^{2+} ion is very unstable, which is easy to be oxidized and form $Fe(OH)_3$ in basic solution [43]. The $Fe(OH)_3$ is difficult to be completely reduced under the experimental condition, so the Fe_3O_4 phase is probably coming from the decomposing of $Fe(OH)_3$ under heat treatment. Furthermore, clear carbon peaks were not observed in the two samples, illustrating that the prepared hollow carbon spheres are amorphous.

The morphologies and microstructures of sample HC-800 and its magnetic metal composites were investigated by TEM, HRTEM and SEM. The monodisperse HMCSs with diameters of 300–680 nm were successfully prepared as shown in Figs. 3a and S1 of the 'ESI.' The hollow morphology and the radial pore channels can be clearly observed, and the thicknesses of the mesoporous shells are 50–90 nm from the TEM image in Fig. S1b. The similar
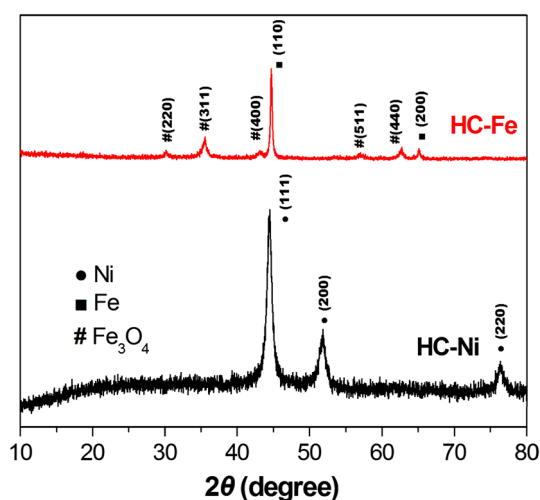
morphologies from TEM can be observed for samples HC-700 and HC-900 (not listed here). Figure 3b shows the TEM image of HMCSs with Ni plating (sample HC–Ni). It can be seen that Ni nanoparticles are homogeneously distributed on the whole hollow carbon particles. The same result is also confirmed by the SEM image as displayed in Fig. S1d. It can be observed that the surfaces of HC–Ni microspheres are rougher than those of HC-800 (Fig. S1a), which should owe to the coating of metal Ni. The microstructure information of HC–Ni is shown in HRTEM image in Fig. 3c. The measured interplanar distance of 0.20 nm can well match with the d-spacing of (111) planes of fcc-Ni. For sample HC–Fe, the TEM images show that the HMCSs are not only coated by nanoparticles but also thin flakes as shown in Figs. 3d and S1g. The HRTEM images display that the interplanar distances of 0.20 nm (Fig. 3e) and 0.25 nm (Fig. 3f) are corresponding to the d-spacing of (110) planes of bcc-Fe and (311) planes of fcc-Fe_3O_4. The results of microstructure are just consistent with those of XRD.

The elemental composition of HC–Ni and HC–Fe composites was acquired by scanning transmission electron microscope (STEM) technology as shown in Fig. 4. The results of elemental mapping clearly indicate the hollow carbon shells with mesoporous structure (Fig. 4b, e) and the homogenous deposition of Ni (Fig. 4c) and Fe (Fig. 4f) on the HMCSs. Additionally, the presence of Ni in HC–Ni and Fe in HC–Fe is also confirmed by energy-dispersive X-ray (EDX) spectrometric analysis as shown in Fig. S2.

Nitrogen adsorption–desorption isotherms of these HMCSs and their magnetic composites can be identified as a type IV isotherm with mesopore hysteresis loop, as shown in Fig. 5a. These characteristic isotherms should derive from the mesoporous structure of carbon shells. The BET specific surface areas (S_{BET}), total pore volumes (V_{pore}) and average pore sizes of these samples are presented in Table 1. The S_{BET} and V_{pore} of HC-700 and HC-800 are comparable; however, the S_{BET} and V_{pore} of HC-900 dramatic increase and the S_{BET} and V_{pore} of HC–Ni and HC–Fe decrease with metal coating on HMCSs. Moreover, as shown in Fig. 5b, the pore size distributions derived from adsorption branches by BJH model indicate that the largest pore size (8.0 nm) can be obtained at the carbonization temperature of 800 °C (HC-800). When the carbonization temperature rises up to 900 °C, the pore size drops to 6.1 nm, indicating the

Figure 2 XRD patterns of HC–Ni and HC–Fe.
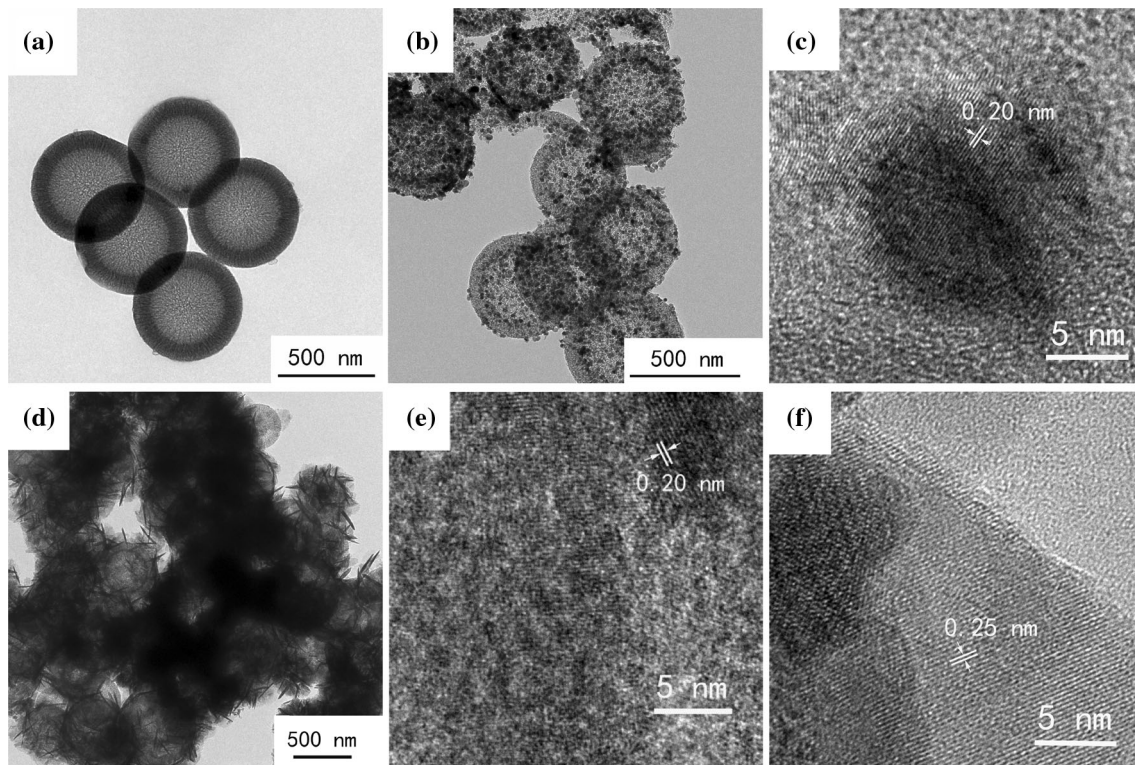
Figure 3 TEM images of HC-800 (**a**), HC–Ni (**b**) and HC–Fe (**d**), and HRTEM images of HC–Ni (**c**) and HC–Fe (**e, f**).

temperature-induced structural shrinkage. Compared with HC-800, the HC–Ni and HC–Fe (Ni and Fe plating on HC-800) show smaller pore diameter, which can partly attribute to the magnetic metal nanoparticles embedding into the mesopores and interior voids in HMCSs.

Magnetic properties

The magnetic hysteresis loops of samples HC–Ni and HC–Fe at room temperature with a maximum applied field of 10 kG are presented in Fig. 6a. The values of saturation magnetization (M_s) are 16.6 emu/g for HC–Ni and 74.8 emu/g for HC–Fe, respectively. The smaller M_s values than those of corresponding bulk materials (55 emu/g of Ni and 220 emu/g of Fe) are subject to nonmagnetic carbon and nanosize of magnetic metal particles [44, 45]. The coercivity (H_c) is 53.2 G for HC–Ni and 114.3 G for HC–Fe as shown in Fig. 6b. Generally, the strong magnetic loss would profit from high initial permeability (μ_i). The μ_i is related to the M_s and H_c, and higher M_s and lower H_c are beneficial to the improvement in the μ_i [46], which is predicting higher magnetic loss of HC–Fe than that of HC–Ni.

Dielectric and microwave absorption properties of HMCSs

Figure 7a, b shows the frequency dependence of relative complex permittivity ($\varepsilon_r = \varepsilon' - j\varepsilon''$) of the HMCSs/paraffin composites with 10 wt% of HMCSs in the frequency range of 2–18 GHz. It can be observed that the values of real part ε' (Fig. 7a) and imaginary part ε'' (Fig. 7b) gradually decrease with the increase in frequency for each HMCSs composite. The maximum values of ε' and ε'' are 7.6 and 4.2 at 2.0 GHz for HC-700, 16.6 and 9.4 for HC-800 and 25.7 and 22.0 for HC-900. The minimum values of ε' and ε'' are 4.2 and 1.9 at 18 GHz for HC-700, 8.3 and 4.9 for HC-800 and 11.3 and 8.1 for HC-900, respectively. It can also found that both of ε' and ε'' of the HMCSs composites increase with the increasing carbonization temperature at each frequency point, which should attribute to the higher degree of graphitization of carbon at higher temperature [39, 47]. In order to compare the dielectric loss properties of the HMCSs composites, the variation in the dielectric loss factor ($\tan\delta_e = \varepsilon''/\varepsilon'$) with frequency is shown in Fig. 7c. It can be also found that the $\tan\delta_e$ increases with the increasing carbonization temperature and
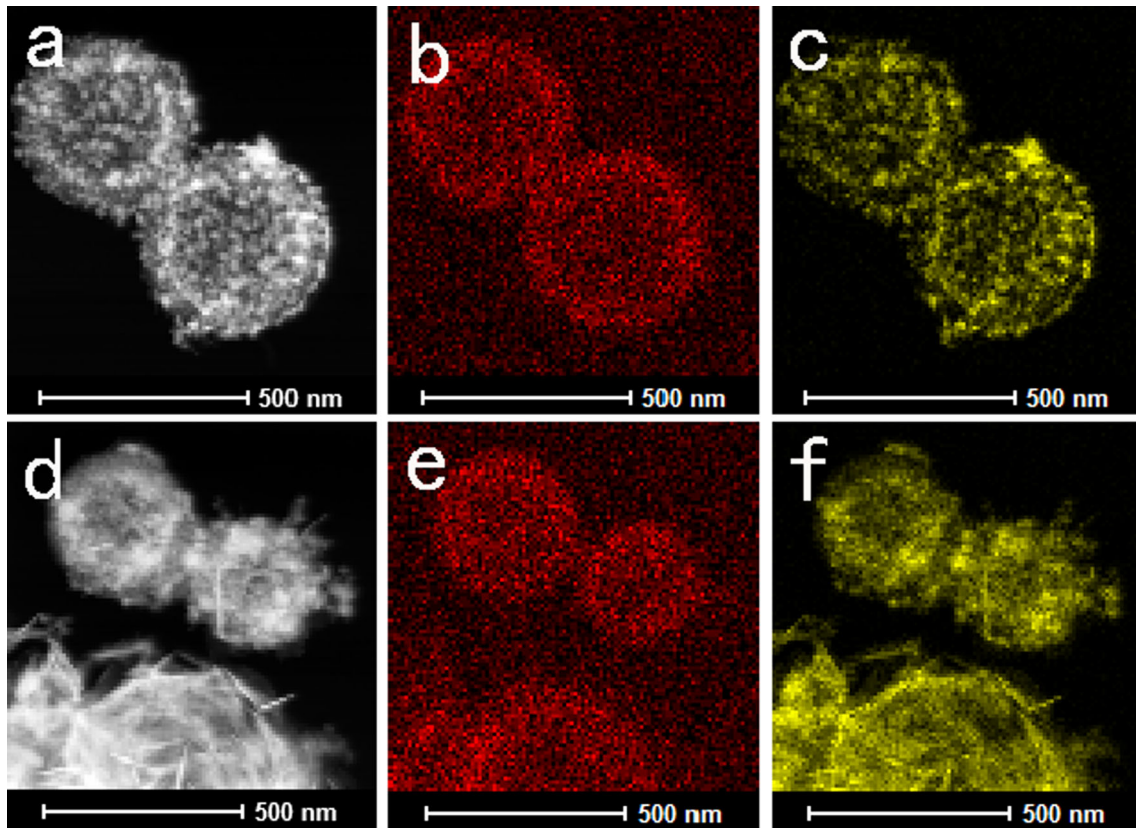
Figure 4 STEM images of HC–Ni (**a**) and HC–Fe (**d**), and elemental mapping for C of HC–Ni (**b**) and HC–Fe (**e**) and Ni of HC–Ni (**c**) and Fe of HC–Fe (**f**).
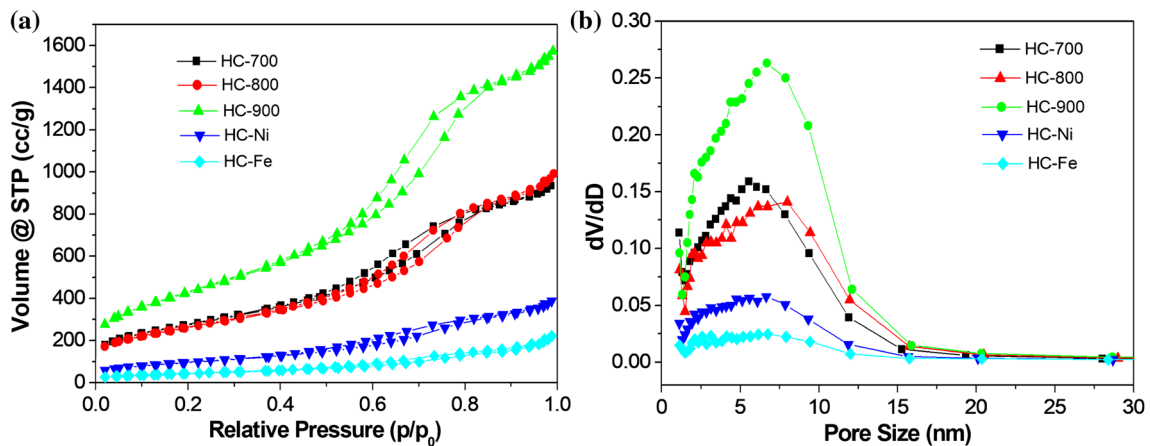
Figure 5 N$_2$ adsorption–desorption isotherms (**a**) and pore size distribution curves (**b**) of the samples.

two dielectric loss peaks can be observed in each curve. The two loss peaks in each curve locate in the same frequency, suggesting the same dielectric loss mechanism for the HMCSs composites. The dielectric loss properties may be explained by the Debye relaxation equation, which is provided in 'ESI.' According to Eq. (2) in 'ESI,' higher conductivity

should correspond to higher ε'', indicating high ε'' partly resulting from the high degree of graphitization of carbon at high temperature. To investigate the dielectric loss mechanism of the HMCSs composites, the curves of ε' versus ε'' are plotted as shown in Fig. 8, where one relaxation process usually corresponds to one semicircle (Cole–Cole semicircle). It

Table 1 Surface areas, total pore volumes and pore sizes of the samples

Samples	S_{BET} (m^2 g^{-1})	V_{pore} (cm^3 g^{-1})	Pore size (nm)
HC-700	979	1.446	5.5
HC-800	930	1.535	8.0
HC-900	1549	2.435	6.7
HC–Ni	348	0.5992	6.7
HC–Fe	157	0.3430	6.8

can be found that there are two semicircles in each curve, which suggests that multiple relaxation processes occurred in these HMCSs composites. Besides conductivity loss, the dielectric loss behaviors are also decided by polarization loss including ionic polarization, electronic polarization, dipole orientation polarization and interfacial polarization. Because ionic polarization and electronic polarization usually occur very fast (10^{-15}–10^{-13} s), their contribution to dielectric loss can be excluded. Thus, the multiple relaxation processes should attribute to interfacial

polarization deriving from different conductivity among paraffin, carbon and air in pores and dipole orientation polarization resulting from abundant bound charges accumulated by the defects and residual groups in the low-crystalline carbon [40, 46].
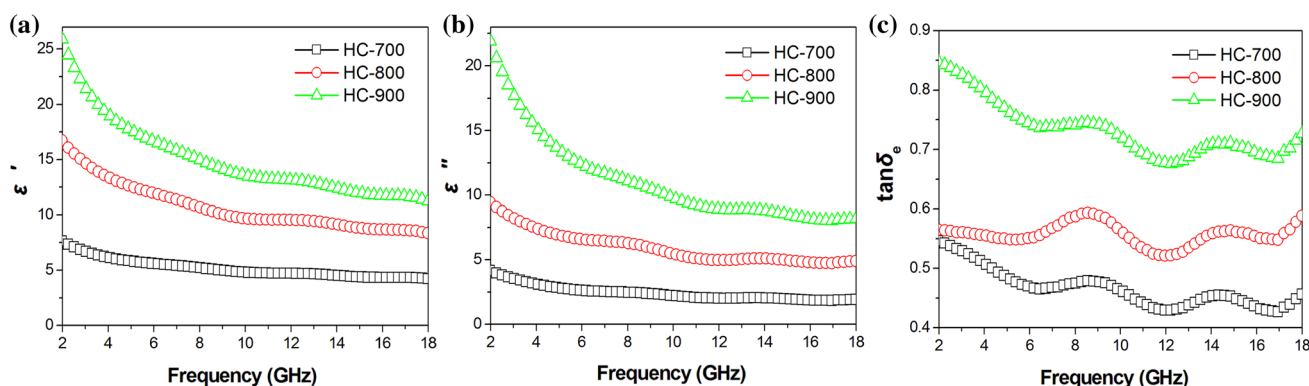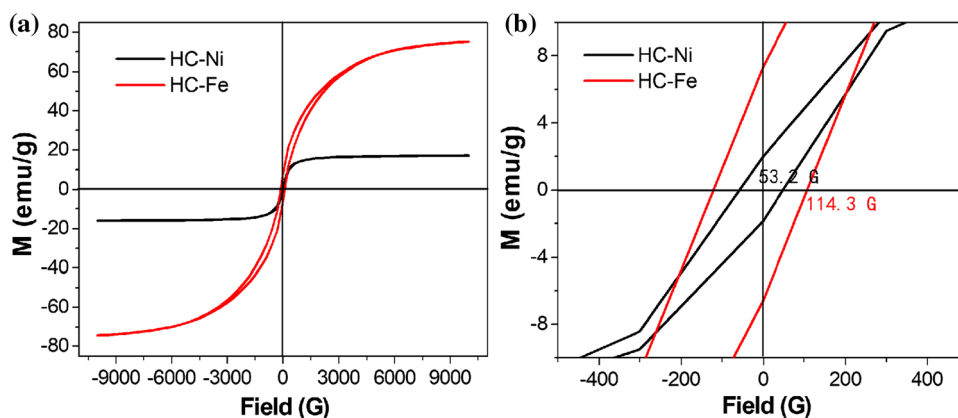
On the basis of relative complex permittivity and permeability, the reflection loss (RL) of the single-layer absorber with a perfect metal-backed plate can be deduced from the transmission line theory.

$$RL\,(dB) = 20\lg\left|\frac{Z_{in} - 1}{Z_{in} + 1}\right| \qquad (1)$$

where Z_{in} is the relative input impedance of absorber at air/absorber interface, which is given by

$$Z_{in} = \sqrt{\frac{\mu_r}{\varepsilon_r}}\tanh\left(j\frac{2\pi fd}{c}\sqrt{\mu_r\varepsilon_r}\right) \qquad (2)$$

where d is the thickness of absorber, f is the frequency and c is the velocity of light in free space. Figure 9 shows the planar RL maps of the HMCSs composites with varied thickness from 0.5 to 5.5 mm. The three-

Figure 6 Hysteresis loops of HC–Ni and HC–Fe at room temperature.

Figure 7 Frequency dependence of real part (**a**) and imaginary part (**b**) of relative complex permittivity and dielectric loss factor (**c**) of HC-700, HC-800 and HC-900 composites.
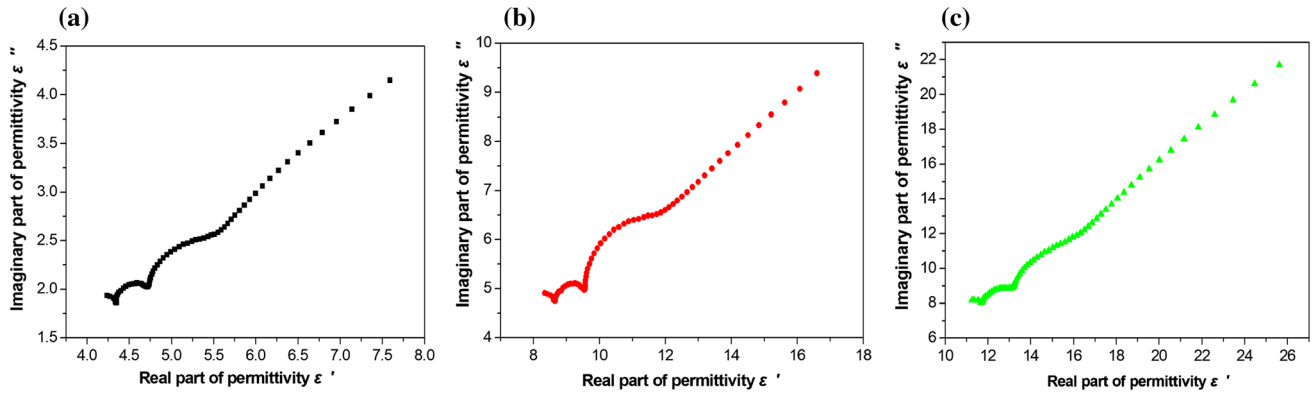
Figure 8 Plots of ε'' versus ε' of HC-700 (**a**), HC-800 (**b**) and HC-900 (**c**) composites.
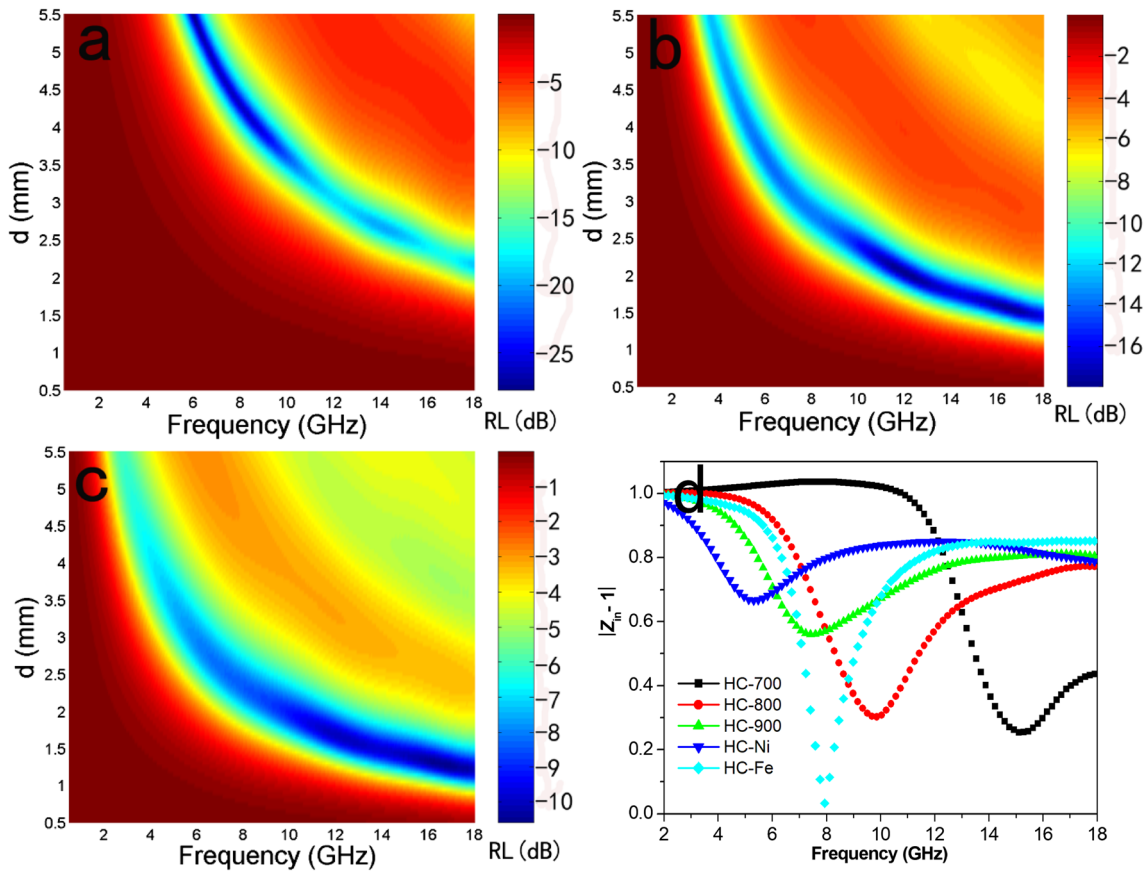
Figure 9 Reflection loss maps of HC-700 (**a**), HC-800 (**b**) and HC-900 (**c**) composites with varied absorber thickness from 0.5 to 5.5 mm and the frequency dependence of Modulus of $Z_{in} - 1$ of different HMCSs composites with a thickness of 2.5 mm (**d**).

dimensional (3-D) RL images and typical RL plots with some specific thickness are also shown in Fig. S3 of 'ESI.' For the HC-700 composite, the minimum RL value is -26.4 dB at 6.7 GHz with thickness of 5.0 mm and the maximum effective absorption bandwidth (less than -10 dB) reaches 5.5 GHz

(12.5–18 GHz) with thickness of 2.5 mm (Fig. S3b). For the HC-800 composite, the minimum RL value of -17.9 dB at 12.2 GHz and the effective absorption bandwidth of 4.1 GHz (10.7–14.8 GHz) with a thickness of 2.0 mm (Fig. S3d) can be obtained. However, there is not any RL value lower than -10 dB for the

HC-900 composite, indicating poor microwave absorption performance. Although HC-900 composites have the highest dielectric loss factor among these composites as shown in Fig. 7c, higher dielectric loss cannot guarantee better microwave absorption in any frequency from the above RL results because absorption property depends on not only dielectric loss and magnetic loss but also impedance matching at air/absorbers interface. For nonmagnetic HMCSs composites, higher complex permittivity could result in poorer impedance matching; thus, most of the incident electromagnetic waves will be reflected at the front surface of absorbers, rather than transmitted into the absorber and attenuated by absorbers. However, it is difficult to evaluate the characteristic impedance of materials because it is an imaginary number. Here the modulus of $Z_{in} - 1$ is used to evaluate the RL properties of the composites [37]. According to Eq. (1), the nonreflecting condition is that the modulus of $Z_{in} - 1$ is equal to zero; accordingly, strong absorption can produce when the modulus of $Z_{in} - 1$ is closer to zero. Here an example of frequency dependence of the modulus of $Z_{in} - 1$ for these composites with thickness of 2.5 mm is given in Fig. 9d. The result exhibits that the modulus of $Z_{in} - 1$ of HC-700 composites closer to zero than other two composites in high frequency range, presenting that the characteristic impedance is matched well in the high frequency range. For HC-800 composites, better impedance matching is in the medium frequency range. However, the modulus of $Z_{in} - 1$ of HC-900 composite is far from zero in the whole frequency range, implying poor microwave absorption property. Moreover, as shown in Fig. 9a–c, the RL peaks shift to low frequency with thickness increasing for each composite. The location of RL peak is related to the set thickness, frequency and electromagnetic parameters of absorbers. It can be deduced by formula [48]

$$d_{m} = \frac{n\lambda_{m}}{4} = \frac{nc}{4f_{m}\sqrt{|\varepsilon_r\mu_r|}} \quad (n = 1, 3, 5, \ldots) \quad (3)$$

where d_m is the matching thickness and λ_m and f_m are the wavelength and frequency in RL peak position, respectively. Meanwhile, the formula can also explain why RL peaks also shift to low frequency with the increasing of modulus of ε_r for different composite with the same thickness. The microwave absorption properties of these composites are also summarized in Table S1 of 'ESI.'

Microwave absorption properties of magnetic HMCSs composites

In order to enhance the microwave magnetic loss, the HMCSs are coated with magnetic metal Ni and Fe by electroless plating method. Figures 10a, b, S4a and S4b show the frequency dependence of relative complex permittivity of the magnetic HMCSs/paraffin composites with 40 wt% of magnetic HMCSs composites. As shown in Fig. 10a, b, the values of real part ε' and imaginary part ε'' of HC–Ni gradually decline with the increase in frequency, whose results are similar to those HMCSs/paraffin composites as shown in Fig. 7a, b. However, for the HC–Fe composite, the values of ε'' increase slightly with the increase in frequency. It can be also observed that the values of ε' and ε'' of HC–Ni composite are higher than those of HC–Fe composite at each frequency point, which mainly derives from the higher carbon content in HC–Ni composite. According to the mass of the obtained products and EDX spectrum in Fig. S2, the carbon content is about 42 wt% in HC–Ni and 30 wt% in HC–Fe. Therefore, the carbon content is 16.8 wt% in HC–Ni/paraffin and 12.0 wt% in HC–Fe/paraffin composite, respectively. The similar variation in ε' and ε'' of magnetic HC-700 and HC-900 composites with frequency is also found from Fig. S4a and S4b of 'ESI.' Generally, the values of ε' and ε'' of the magnetic HMCSs composites go up with the increasing carbonization temperature. However, an exception is observed in the ε'' of the magnetic HMCSs/Fe composites, where the values of ε'' of HC–Fe are lower than those of HC-700–Fe as shown in Figs. 10b and S4b. Figure 10c shows the variation in $\tan\delta_e$ with frequency. It is found that the HC–Ni composite displays higher dielectric loss than HC–Fe composite and two dielectric loss peaks can be observed in each curve. The locations of two peaks are the same as those in HNCSs composites (Fig. 7c), suggesting the similar dielectric loss mechanism for both of the HMCSs composites and magnetic HMCSs composites. Figures 10d, e, S4c and S4d display the frequency dependence of relative complex permeability ($\mu_r = \mu' - j\mu''$) of the magnetic HMCSs composites. It is found that magnetic performances of the HMCSs composites are obviously enhanced with introducing of Ni and Fe particles as shown in Fig. 10d, e. The values of real part μ' of HC–Ni composite decrease from 1.16 at 2 GHz to 1.04 at 7.3 GHz and then go up with fluctuation in the following frequency range. The
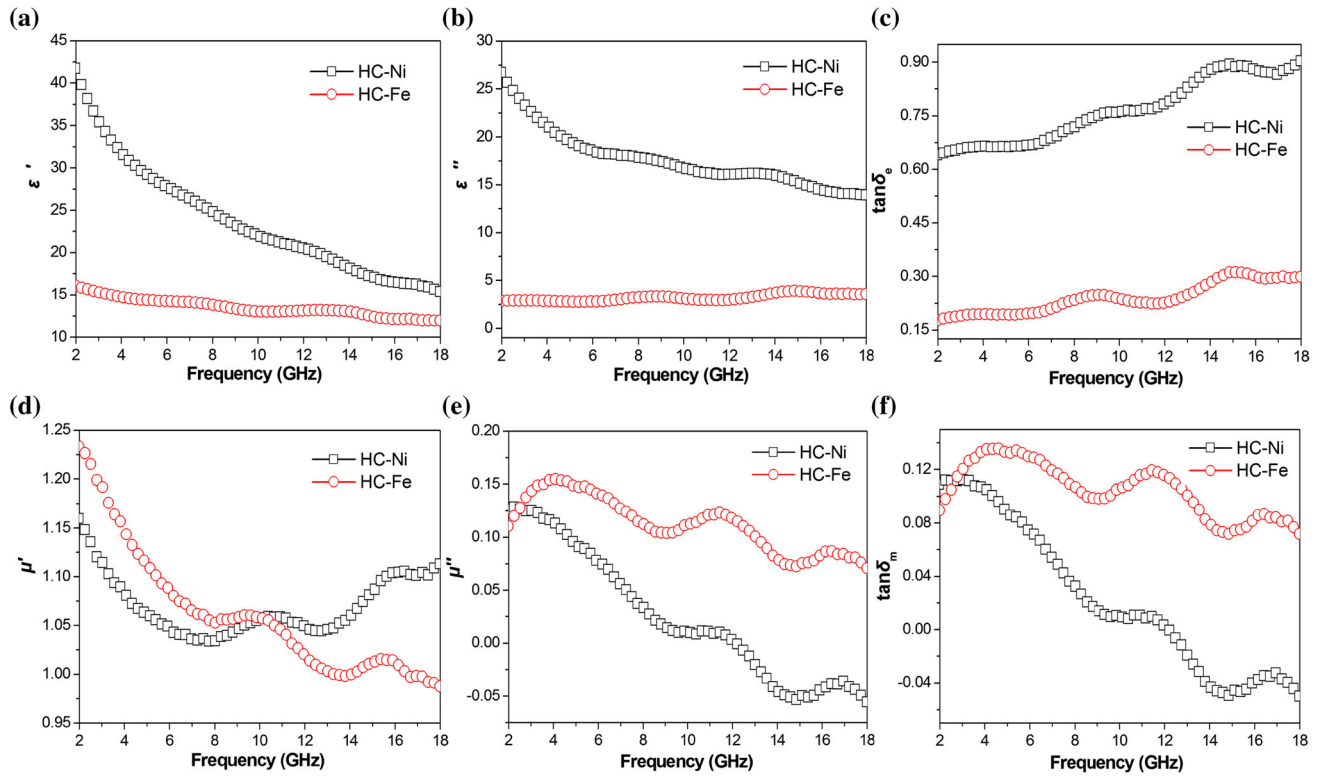
Figure 10 Frequency dependence of relative complex permittivity (**a**, **b**), relative complex permeability (**d**, **e**), dielectric loss factor (**c**) and magnetic loss factor (**f**) of HC–Ni and HC–Fe composites.

values of μ' of HC–Fe composite dramatically decline from 1.24 at 2 GHz to 1.05 at 7.8 GHz and then moderately decrease with fluctuation. The values of μ' of HC–Fe composite are higher than those of HC–Ni composite before 10.0 GHz, and inverse result occurs hereafter. The values of imaginary part μ'' of HC–Fe composite are higher than those of HC–Ni composite almost in the whole frequency range from Fig. 10e, indicating stronger magnetic loss of HC–Fe composite. The result is also confirmed by magnetic loss factor ($\tan\delta_m = \mu''/\mu'$) in Fig. 10f. Three obvious peaks can be observed at 4.4 GHz, 11.4 GHz and 16.2 GHz in the $\tan\delta_m$ curve of HC–Fe composite, indicating strong resonance absorption. It is well known that magnetic loss mainly results from hysteresis, domain wall resonance, eddy current loss and ferromagnetic resonance [49]. The hysteresis happens in strong field, and the domain wall resonance usually occurs at MHz frequency. Therefore, the two magnetic losses can be easily excluded here. The contribution of eddy current loss to μ'' is related to the electric conductivity (σ) and the diameter (d) of nanoparticles [50]. If μ'' derives only from eddy current loss, the value of $\mu''(\mu')^{-2}f^{-1}$

($= 2\pi\mu_0 d^2\sigma/3$) should be a constant in the whole frequency range [51]. Figure 11 shows the frequency dependence of $\mu''(\mu')^{-2}f^{-1}$ of HC–Ni and HC–Fe composites. It is found that the values of $\mu''(\mu')^{-2}f^{-1}$ of
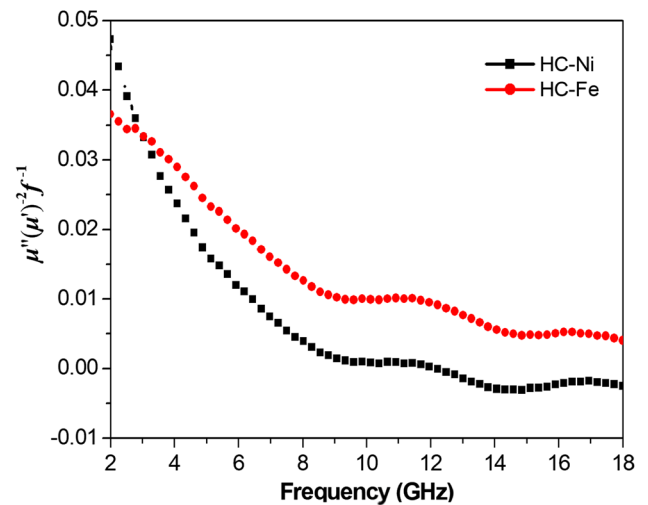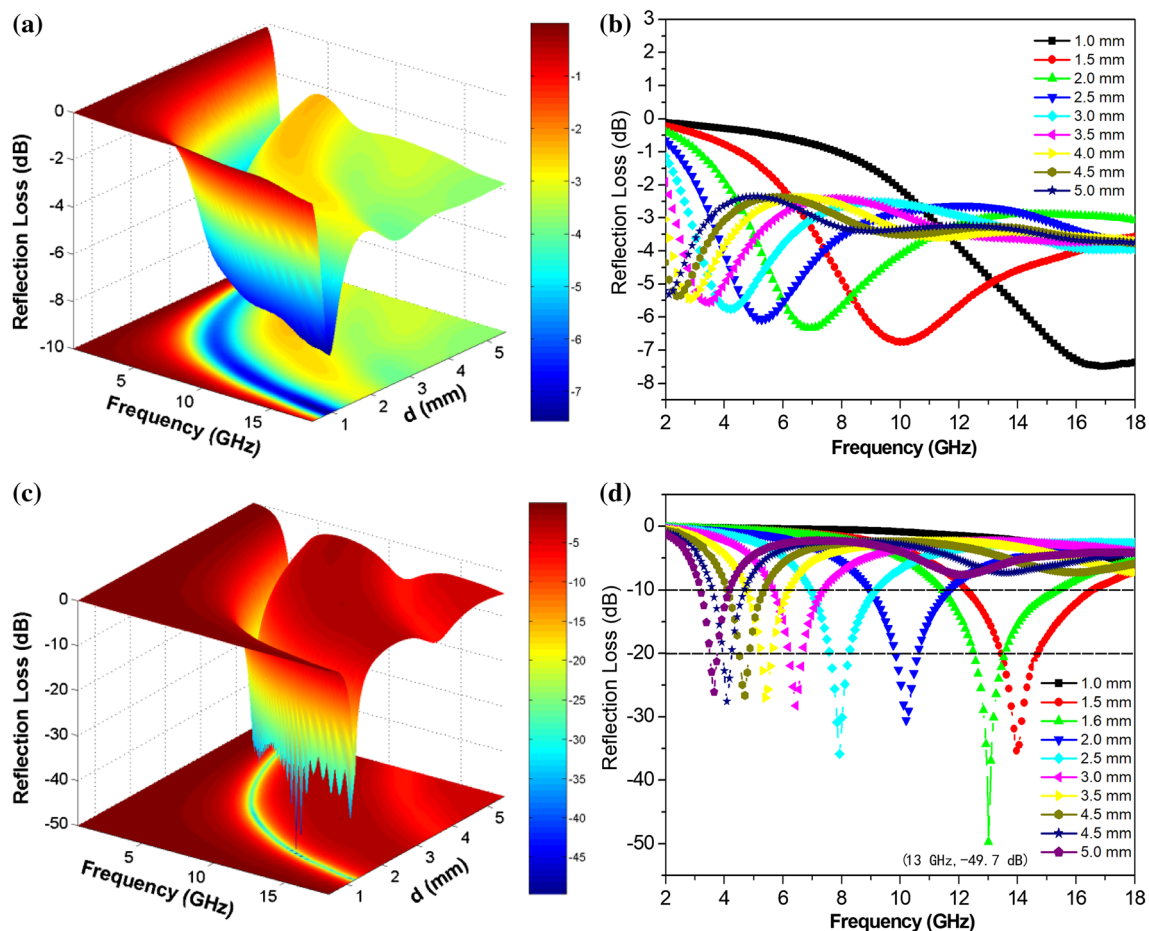

Figure 11 Frequency dependence of $\mu''(\mu')^{-2}f^{-1}$ of HC–Ni and HC–Fe composites.

the two composites dramatically decline before 9.3 GHz and then slightly decline in following frequency range. Two peaks can be observed for each composite, confirming that the magnetic loss is caused by not only eddy current but also ferromagnetic resonance. As observed from Fig. S4c and S4d, the magnetic HMCSs carbonized at 700 °C and 900 °C composites display similar frequency dependence of μ' and μ'' to HC–Ni and HC–Fe except for HC-900–Ni composite with lower μ' values.

Figures 12 and S5 show the 3-D RL images with projection planes of the magnetic HMCSs composites with varied thickness from 0.5 to 5.5 mm and typical RL plots with some specific absorber thickness. As shown in Fig. 12a, b, the peak value of RL of HC–Ni composite is larger than − 10 dB for each thickness, indicating poor absorption property of the HC–Ni composite. However, the HC–Fe composite displays excellent microwave absorption property. The peak

value of RL is less than − 20 dB for each thickness of greater than 1.2 mm. The minimum RL value reaches − 49.7 dB at 13 GHz (as shown in Fig. 12d), and the effective absorption bandwidth is 4.0 GHz (11.4–15.4 GHz) for the thickness of 1.6 mm. The maximum effective absorption bandwidth reaches 4.3 GHz (12.3–16.6 GHz) with a thickness of 1.5 mm. From Figs. 12c and S3a, it can be found that HC–Fe composite reveals more excellent microwave absorption property than HC-700 composite. The complex permittivity of HC–Fe composite is comparable to those of HC-700 composite as shown in Figs. 7 and 10; however, the complex permeability of HC–Fe composite is higher because of the introducing of magnetic Fe particles, resulting in higher magnetic loss and better impedance matching. Therefore, the excellent absorption property of the HC–Fe composite derives from the synergistic effect among dielectric loss, magnetic loss and impedance

Figure 12 3-D reflection loss images (a, c) and typical reflection loss plots (b, d) with some specific absorber thickness of HC–Ni (a, b) and HC–Fe (c, d) composites.

matching. The frequency dependence of the modulus of $Z_{in} - 1$ for the two magnetic composites with thickness of 2.5 mm is also shown in Fig. 9d. The result shows that the modulus of $Z_{in} - 1$ of HC–Ni composite is far from zero in the whole frequency range, indicating that the characteristic impedance is not matched well. For HC–Fe composite, the modulus of $Z_{in} - 1$ is very close to zero at 8 GHz or so, indicating good impedance matching in the frequency. However, as shown in Fig. S5, the HC-700–Ni, HC-700–Fe, HC-900–Ni and HC-900–Fe composites show weaker microwave absorption than corresponding HC-700 and HC-900 composites. The minimum RL is − 13.6 dB at 18 GHz, − 12.3 dB at 11.5 GHz, − 3.1 GHz at 2 GHz and − 4.8 dB at 15.6 GHz for HC-700–Ni, HC-700–Fe, HC-900–Ni and HC-900–Fe composites, respectively. The weak reflection losses mainly derive from the poor impedance matching of the magnetic HMCSs composites with higher complex permittivity than corresponding HMCSs as shown in Figs. 7 and S4.

Conclusions

In summary, monodisperse HMCSs with the diameters of 300–680 nm and mesoporous shell thicknesses of 50–90 nm have been successfully synthesized via a 'polymerization–pyrolysis–etching' route. The complex permittivity results show that dielectric loss of the HMCSs/paraffin composites increases with the increase in carbonization temperature. However, the HMCSs composite with the highest dielectric loss factor does not show superior microwave absorption property due to poor impedance matching at air/absorber interface. The minimum RL value is − 26.4 dB at 6.7 GHz with a thickness of 5.0 mm, and the maximum effective absorption bandwidth less than − 10 dB reaches 5.5 GHz (12.5–18 GHz) with a thickness of 2.5 mm for the HC-700 composite. To enhance the magnetic loss and improve the impedance matching of HMCSs, electroless plating methods are employed to deposit Ni and Fe nanoparticles on the surface of HMCSs. The lightweight Fe/HMCSs composite shows excellent microwave absorption property. The peak value of RL is less than − 20 dB at each set thickness of greater than 1.2 mm. The minimum RL value reaches − 49.7 dB at 13.0 GHz, and the effective absorption bandwidth is 4.0 GHz (11.4–15.4 GHz) for the thickness of only 1.6 mm.

Compliance with ethical standards

Conflict of interest The authors declare there is no any commercial or associative interest that represents a conflict of interest in connection with the work submitted.

Electronic supplementary material: The online version of this article (https://doi.org/10.1007/s10853-018-3100-z) contains supplementary material, which is available to authorized users.

References

[1] Xu Z, Huang YA, Yang Y, Shen JY, Tang T, Huang RS (2010) Dispersion of iron nano-particles on expanded graphite for the shielding of electromagnetic radiation. J Magn Magn Mater 322:3084–3087

[2] Joseph N, Singh SK, Sirugudu RK, Murthy VRK, Ananthakumar S, Sebastian MT (2013) Effect of Silver incorporation into PVDF-barium titanate composites for EMI shielding application. Mater Res Bull 48:1681–1687

[3] Joon S, Kumar R, Singh AP, Shukla R, Dhawan SK (2015) Fabrication and microwave shielding properties of free standing polyaniline-carbon fiber thin sheets. Mater Chem Phys 160:87–95

[4] Fu JY, Yang W, Hou LQ, Chen Z, Qiu T, Yang HT, Li YF (2017) Enhanced electromagnetic microwave absorption performance of lightweight bowl-like carbon nanoparticles. Ind Eng Chem Res 56:11460–11466

[5] Zhou C, Geng S, Xu XW, Wang TH, Zhang LQ, Tian XJ, Yang F, Yang HT, Li YF (2016) Lightweight hollow carbon nanospheres with tunable sizes towards enhancement in microwave absorption. Carbon 108:234–241

[6] Qiang R, Du YC, Wang Y, Wang N, Tian CH, Ma J, Xu P, Han XJ (2016) Rational design of yolk–shell C@C microspheres for the effective enhancement in microwave absorption. Carbon 98:599–606

[7] Qin F, Brosseau C (2012) A review and analysis of microwave absorption in polymer composites filled with carbonaceous particles. J Appl Phys 111:061301

[8] Zhang YN, Liu W, Quan B, Ji GB, Ma JN, Li DR, Meng W (2017) Achieving the interfacial polarization on C/Fe₃C heterojunction structures for highly efficient lightweight microwave absorption. J Colloid Interface Sci 508:462–468

[9] Li YX, Liu RG, Pang XY, Zhao XN, Zhang YH, Qin GW, Zhang XF (2018) Fe@C nanocapsules with substitutional sulfur heteroatoms in graphitic shells for improving microwave absorption at gigahertz frequencies. Carbon 126:372–381

[10] Wu T, Liu Y, Zeng X, Cui TT, Zhao YT, Li YN, Tong GX (2016) Facile hydrothermal synthesis of Fe₃O₄/C core–shell nanorings for efficient low-frequency microwave absorption. ACS Appl Mater Interfaces 8:7370–7380

[11] Liu DW, Qiang R, Du YC, Wang Y, Tian CH, Han XJ (2018) Prussian blue analogues derived magnetic FeCo alloy/carbon composites with tunable chemical composition and enhanced microwave absorption. J Colloid Interface Sci 514:10–20

[12] Li YX, Wang JY, Liu RG, Zhao XN, Wang XJ, Zhang XF, Qin GW (2017) Dependence of gigaherze microwave absorption on the mass fraction of Co@C nanocapsules in composites. J Alloys Compd 724:1023–1029

[13] Wan YZ, Xiao J, Li CZ, Xiong GY, Guo RS, Li LL, Han M, Luo HL (2016) Microwave absorption properties of FeCo-coated carbon fibers with varying morphologies. J Magn Magn Mater 399:252–259

[14] Shah A, Ding A, Wang YH, Zhang L, Wang DX, Muhammad J, Huang H, Duan YP, Dong XL, Zhang ZD (2016) Enhanced microwave absorption by arrayed carbon fibers and gradient dispersion of Fe nanoparticles in epoxy resin composites. Carbon 96:987–997

[15] Salimkhani H, Palmeh P, Khiabani AB, Hashemi E, Matinpour S, Slimkhani H, Asl MS (2016) Eletrophoretic deposition of spherical carbonyl iron particles on carbon fibers as a microwave absorbent composite. Surf Interfaces 5:1–7

[16] Che RC, Peng LM, Duan XF, Qin C, Liang XL (2004) Microwave absorption enhancement and complex permittivity and permeability of Fe encapsulated within carbon nanotubes. Adv Mater 16:401–405

[17] Lin L, Xing HL, Shu RW, Wang L, Ji XL, Tan DX, Gan Y (2015) Preparation and microwave absorption properties of multi-walled carbon nantubes decorated with Ni-doped SnO₂ nancrystals. RSC Adv 5:94539–94550

[18] Li N, Huang GW, Li YQ, Xiao HM, Feng QP, Hu N, Fu SY (2017) Enhanced microwave absorption performance of coated carbon nanotubes by optimizing the Fe₃O₄ nanocoating structure. ACS Appl Mater Interfaces 9:2973–2983

[19] Yang QX, Liu L, Hui D, Chipara M (2016) Microstructure, electrical conductivity and microwave absorption properties of γ-FeNi decorated carbon nanotube composites. Compos Part B 87:256–262

[20] Cao MS, Yang J, Song WL, Zhang DQ, Wen B, Jin HB, Hou ZL, Yuan J (2012) Ferroferric oxide/multiwalled carbon nanotube vs. polyaniline/ferroferric oxide/multiwalled carbon nanotube multiheterostructures for highly effective microwave absorption. ACS Appl Mater Interfaces 4:6949–6956

[21] Liu ZF, Xing HL, Liu Y, Wang H, Jia HX, Ji XL (2017) Hydrothermally synthesized Zn ferrite/multi-walled carbon nanotubes composite with enhanced electromagnetic-wave absorption performance. J Alloys Compd 731:745–752

[22] Liu X, Wang LS, Ma YT, Qiu YL, Xie QS, Chen YZ, Peng DL (2018) Facile synthesis and microwave absorption properties of yolk–shell ZnO-Ni-C/RGO composite materials. Chem Eng J 333:92–100

[23] Zong M, Huang Y, Zhang N, Wu HW (2015) Influence of (RGO)/(ferrite) ratios and graphene reduction degree on microwave absorption properties of graphene composites. J Alloys Compd 644:491–501

[24] Zhang XJ, Wang GS, Cao WQ, Wei YZ, Liang JF, Guo L, Cao MS (2014) Enhanced microwave absorption property of reduced graphene oxide (RGO)-MnFe₂O₄ nanocomposites and polyvinylidene fluoride. ACS Appl Mater Interfaces 6:7471–7478

[25] Shen GZ, Xu YW, Liu B, Du P, Li Y, Zhu J, Zhang D (2016) Enhanced microwave absorption properties of N-doped ordered mesoporous carbon plated with metal Co. J Alloys Compd 680:553–559

[26] Wu HJ, Wang LD, Wang YM, Guo SL, Shen ZY (2012) Enhanced microwave performance of highly ordered mesoporous carbon coated by Ni₂O₃ nanoparticles. J Alloys Compd 525:82–85

[27] Li GX, Guo YX, Sun X, Wang T, Zhou JH, He JP (2012) Synthesis and microwave absorbing properties of FeNi alloy incorporated ordered mesoporous carbon–silica nanocomposite. J Phys Chem Solids 73:1268–1273

[28] Shi GM, Zhang B, Wang XL, Fu YH (2016) Enhance microwave absorption properties of core double-shell type Fe@C@BaTiO₃ nanocapsules. J Alloys Compd 655:130–137

[29] Wang C, Xu TT, Wang CA (2016) Microwave absorption properties of C/(C@CoFe) hierarchical core–shell spheres synthesized by using colloidal spheres as templates. Ceram Int 42:9178–9182

[30] Khani O, Shoushtari MZ, Jazirehpour M, Shams MH (2016) Effect of carbon shell thickness on the microwave absorption

of magnetite-carbon core–shell nanoparticles. Ceram Int 42:14548–14556

[31] Zhao X, Li W, Zhang SS, Liu LH, Liu SX (2015) Facile fabrication of hollow and honeycomb-like carbon spheres from liquefied larch sawdust via ultrasonic spray pyrolysis. Mater Lett 157:135–138

[32] Ma FW, Zhao H, Sun LP, Li Q, Huo LH, Xia T, Gao S (2012) A facile route for nitrogen-doped hollow graphitic carbon sphere with superior performance in supercapacitors. J Mater Chem 22:13464–13468

[33] Fang Y, Gu D, Zou Y, Wu ZX, Li FY, Che RC, Deng YH, Tu B, Zhao DY (2010) A low-concentration hydrothermal synthesis of biocompatible ordered mesoporous carbon nanospheres with tunable and uniform size. Angew Chem Int Ed 49:7987–7991

[34] Meng Y, Gu D, Zhang FQ, Shi YF, Cheng L, Feng D, Wu ZX, Chen ZX, Wan Y, Stein A, Zhao DY (2006) A family of highly ordered mesoporous polymer resin and carbon structures from organic–organic self-assembly. Chem Mater 18:4447–4464

[35] Tanaka S, Nakao H, Mukai T, Katayama Y, Miyake Y (2012) An experimental investigation of the ion storage/transfer behavior in an electrical double-layer capacitor by using monodisperse carbon spheres with microporous structure. J Phys Chem C 116:26791–26799

[36] Han Y, Dong XT, Zhang C, Liu SX (2012) Hierarchical porous carbon hollow-spheres as a high performance electrical double-layer capacitor materials. J Power Sources 211:92–96

[37] Xu HL, Yin XW, Zhu M, Han MK, Hou ZX, Li XL, Zhang LT, Cheng LF (2017) Carbon hollow microspheres with a designable mesoporous shell for high-performance electromagnetic wave absorption. ACS Appl Mater Interfaces 9:6332–6341

[38] Cheng Y, Li ZY, Li Y, Dai SS, Ji GB, Zhao HQ, Cao JM, Du YW (2018) Rationally regulating complex dielectric parameters of mesoporous carbon hollow spheres to carry out efficient microwave absorption. Carbon 127:643–652

[39] Du YC, Liu T, Yu B, Gao HB, Xu P, Wang JY, Wang XH, Han XJ (2012) The electromagnetic properties and microwave absorption of mesoporous carbon. Mater Chem Phys 135:884–891

[40] Huang YX, Wan Y, Li ZM, Yang Z, Shen CH, He CC (2014) Effect of pore morphology on the dielectric properties of porous carbon for microwave absorption application. J Phys Chem C 118:26027–26032

[41] Zhang HW, Noonan O, Huang XD, Yang YN, Xu C, Zhou L, Yu CZ (2016) Surfactant-free assembly of mesoporous carbon hollow spheres with large tunable pore sizes. ACS Nano 10:4579–4586

[42] Park KY, Han JH, Lee SB, Yi JW (2011) Microwave absorbing hybrid composites containing Ni-Fe coated carbon nanofibers prepared by electroless plating. Compos Part A 42:573–578

[43] Zhang CW, Wang F (2005) Structure and coordination investigation of iron-ion tinting principle in ferreous glass. J Wuhan Univ Technol Mater Sci Ed 20:8–11

[44] Liu X, Guo HZ, Xie QS, Luo Q, Wang LS, Peng DL (2015) Enhanced microwave absorption properties in GHz range of Fe_3O_4/C composite materials. J Alloys Compd 649:537–543

[45] Wu ND, Liu XG, Zhao CY, Cui CY, Xia AL (2016) Effects of particle size on the magnetic and microwave absorption properties of carbon-coated nickel nancapsules. J Alloys Compd 656:628–634

[46] Ding D, Wang Y, Li XD, Qiang R, Xu P, Chu WL, Han XJ, Du YC (2017) Rational design of core–shell Co@C microspheres for high-performance microwave absorption. Carbon 111:722–732

[47] Wang JC, Zhou H, Zhuang JD, Liu Q (2015) Magnetic γ-Fe_2O_3, Fe_3O_4, and Fe nanoparticles confined within ordered mesoporous carbons as efficient microwave absorbers. Phys Chem Chem Phys 17:3802–3812

[48] Liu C, Yuan Y, Jiang JT, Gong YX, Zhen L (2015) Microwave absorption properties of FeSi flaky particles prepared via a ball-milling process. J Magn Magn Mater 395:152–158

[49] Aharoni A (1991) Exchange resonance modes in a ferromagnetic sphere. J Appl Phys 69:7762–7764

[50] Zong M, Huang Y, Zhao Y, Sun X, Qu CH, Luo DD, Zheng JB (2013) Facile preparation, high microwave absorption and microwave absorbing mechanism of RGO-Fe_3O_4 composites. RSC Adv 3:23638–23648

[51] Shen GZ, Mei BQ, Wu HY, Wei HY, Fang XM, Xu YW (2017) Microwave electromagnetic and absorption properties of N-doped ordered mesoporous carbon decorated with ferrite nanoparticles. J Phys Chem C 121:3846–3853